Supplement of

Polar amplification of orbital-scale climate variability in the early Eocene greenhouse world

Chris D. Fokkema et al.

Correspondence to: Chris D. Fokkema (c.d.fokkema@uu.nl)

This PDF file includes:

- Supplementary Text
    - 1. TEX_{86} calibrations
    - 2. Polar amplification assessment
- Supplementary Figures S1 – S9
- Supplementary References

1. TEX_{86} calibrations

The calibration of TEX_{86} to temperature has remained challenging since the proxy was first proposed (Schouten et al., 2002; Hollis et al., 2019). Paleotemperature reconstructions obtained by extrapolation of coupled satellite measurements and surface sediment-derived TEX_{86} ratios are dependent on the chosen calibration model, particularly outside the range of modern ocean temperatures as is the case in many early Paleogene and Mesozoic studies, including this study. The options can be crudely summarized in two choices: linear versus non-linear models, and ocean surface versus subsurface calibrations.

1.1 Calibration shape

Following the original linear TEX_{86}-sea surface temperature (SST) calibration (Schouten et al., 2002), subsequently proposed calibrations include linear (O'Brien et al., 2017), including a spatially varying Bayesian approach ('BAYSPAR') (Tierney and Tingley, 2014), reciprocal (Liu et al., 2009), and exponential (Kim et al., 2010) models. Linear calibrations are typically preferred because they are the simplest models. However, previous work has highlighted that the TEX_{86} describes only a minor component of the response of Thaumarcheotal membrane-lipids to temperature. Rather, the response is dominated by GDGT-0 and crenarchaeol (cren) (Kim et al., 2010; Cramwinckel et al., 2018) which are not incorporated in TEX_{86}, but dominate the isoGDGT temperature response at temperatures above 15 ºC (Kim et al., 2010). If Thaumarchaeota increasingly adapt their membranes using GDGTs that are not included in TEX_{86} at higher temperatures, it would imply that TEX_{86} loses sensitivity to temperature at the higher temperature range (Cramwinckel et al., 2018). This variable degree of (in)sensitivity presumably results in a non-linear relationship over the complete temperature range.

The BAYSPAR calibration partly accounts for variable TEX_{86}-SST relationships by generating linear regressions from selected analog locations from the surface sediment dataset based on given TEX_{86} search tolerances (Tierney and Tingley, 2014). This approach is, however, problematic for datasets that have TEX_{86} values far beyond the surface sediment-derived TEX_{86} values, including that from the Eocene of Site 959. Using BAYSPAR for Paleogene Site 959 TEX_{86} data requires a large search tolerance and results in extrapolation of a constant linear slope based on a rather small number of warmest analog locations. Another linear calibration (O'Brien et al., 2017) uses a linear regression between the global surface sediment TEX_{86} database and SST for regions warmer than 15 °C.

The exponential TEX_{86}^{H}-SST calibration (which excludes (sub)polar and Red Sea data, which have anomalous GDGT distributions) presents a relatively good fit with the non-linear behavior between fractional GDGT abundances and SSTs, and has therefore often been applied in climate reconstructions of past warm intervals (Cramwinckel et al., 2018; Frieling et al., 2019). However, significant drawbacks of the TEX_{86}^{H}-calibration are regression dilution and the residual errors with respect to modern core-top dataset (Tierney and Tingley, 2014).

The modern surface sediment dataset shows that TEX_{86} has very little sensitivity to temperature variability below 15 °C, indicating non-linearity at the low temperature end (Kim et al., 2010). The question is whether the contributions of GDGTs included in TEX_{86} keeps increasing beyond the modern surface sediment dataset, or if this response saturates, as argued previously (Cramwinckel et al., 2018). To further test the viability of linear and exponential relations between TEX_{86} and SST, we analyze the fractional abundances of GDGT-1 versus GDGT-2+GDGT-3+cren' (the constituents of TEX_{86}) in the global surface sediment dataset, for samples from which these are available (Tierney and Tingley, 2015). This analysis shows that the mechanism behind TEX_{86} is nonlinear (Fig. S7). Specifically, at low SSTs, both GDGT-1 and GDGT-2+GDGT-3+cren' increase towards ~15 ºC. At higher SSTs, GDGT-2+GDGT-3+cren' continues to increase while GDGT-1 reaches a local maximum between ~15 ºC and 20 ºC and decreases at higher temperatures. Due to the way that TEX_{86} is calculated, this leads to minimal sensitivity at low temperatures and high sensitivity at higher temperatures. In other words, small changes in GDGT distributions will result in larger changes in TEX_{86} at higher temperatures than at lower temperatures. Because of this, the linear TEX_{86}-SST (here the linear model from O'Brien et al. (2017)) overestimates SSTs in the high TEX_{86} regime of the surface sediment dataset (Fig. S7a, S7c). In contrast, an exponential calibration model (here TEX_{86}^{H}, from Kim et al. (2010) presents a better fit between the high-end surface sediment TEX_{86} and satellite temperature data (Fig. S7b, S7d). This supports a diminishing sensitivity of TEX_{86} to SST at higher temperatures and suggests that the response of linear calibrations overestimates climate variability in reconstructions of warm climates. We therefore argue that extrapolation of this exponential calibration more accurately reconstructs temperature variability in the early Paleogene tropics. In this work we follow the previous inferences (Cramwinckel et al., 2018) about the non-linear relationship between GDGT distributions and temperature, by using exponential calibration models.

1.2 Calibration target depth

Originally, TEX_{86} was calibrated to SST and the temperature at 100 meters depth (Schouten et al., 2002). Today, there is an increasing consensus that pelagic Thaumarchaeota from below the mixed layer are the dominant source to sedimentary GDGT assemblages (Schouten et al., 2002; Kim et al., 2012; Ho and Laepple, 2016; Tierney et al., 2017; Hurley et al., 2018; van der Weijst et al., 2022). Observations show that cell counts of ammonia oxidizing Thaumarchaeota and GDGT abundances peak at the base of the NO_2^- maximum — generally positioned between 50 and 100 m in present-day tropical Atlantic ocean (Zakem et al., 2018) — and only minimally occur within the mixed layer (Massana et al., 2000; Karner et al., 2001; Sinninghe Damsté et al., 2002; Hurley et al., 2018).

The integrated source depths of GDGTs from sediment samples can be estimated using the GDGT-2/GDGT-3 ratio, which shows a correlation with water depth in the core-top dataset (Taylor et al., 2013; van der Weijst et al., 2022; Rattanasriampaipong et al., 2022), but more importantly, the depth in the water column were GDGTs are produced (Hernández-Sánchez et al., 2014; Villanueva et al., 2015; Hurley et al., 2018). These studies show that there is a critical shift in GDGT-2/GDGT-3 values at a water depth of approximately 200 m, after which GDGT-2/GDGT-3 values rapidly increase to values >5 with increasing depth in suspended particulate matter (Hurley et al., 2018). The GDGT-2/GDGT-3 values for the studied interval of Site 959 (values generally below 4, Fig. S2) therefore argue for a dominantly shallow (<200 m) source of the GDGTs, considering integrated depth-GDGT-2/GDGT-3 relationships (van der Weijst et al., 2022). Based on the GDGT-

2/GDGT-3 ratios at this site, and given generally low concentrations of GDGTs shallower than 50 m in the modern open ocean (Hurley et al., 2018), we infer that peak integrated GDGT source depth is between approximately 50 and 200 m water depth for the early Eocene at Site 959.

While a GDGT export zone between 50–200 m is still relatively shallow, it is deep enough to be influenced by upper thermocline waters in many locations, including Site 959 (van der Weijst et al., 2022). Therefore, much of the present-day surface sediment GDGT distributions and those from Site 959 likely dominantly comprise GDGTs that originate from below the mixed layer. Calibrating core-top TEX_{86} data to SST might therefore lead to an unrealistically low temperature-TEX_{86} slope when extrapolating to Eocene temperatures, because the meridional temperature gradient decreases with water depth (Ho and Laepple, 2016).

Several subsurface temperature (SubT) TEX_{86} calibrations exist, targeting different integrated depth ranges and having different calibration model choices. Based on exponential calibration models, (Ho and Laepple, 2016) proposed an ensemble of depth-integrated TEX_{86}-temperature calibrations up to 1000 m depth and both with TEX_{86} as dependent and independent variable. Based on above inferences about peak GDGT source depths at early Eocene Site 959, we choose an equally weighted depth range from this ensemble that targets the interval between 100 and 250 m. This calibration, to which we refer as "$SubT_{100\text{-}250m}$", gives an estimate of shallow subsurface temperature variability which is close to our expected GDGT sourcing depths. It should be considered a conservative estimate (low temperature response with a given TEX_{86} change) by integrating seawater temperatures down to 250 m. Another exponential SubT calibration that focuses on the relevant depth range is published by Kim et al. (2012) (here termed '$SubT_{Kim2012}$'), which is calibrated to the upper 200 m water depth and thus includes the mixed layer, which increases proxy sensitivity.

1.3 Calibration choice for polar amplification assessment

For calculation of PA factors, only calibration slopes are relevant, because the PA factor is independent of reconstructed absolute temperatures. As models show that variability of SST and SubT is equal (Fig. S1b), consistent with data-based estimates (Ho and Laepple, 2016), this allows the in-tandem use of SST and SubT calibrations to calculate PA factors and provide an estimated error range of SST variability. Three exponential calibration models, TEX_{86}^{H}, $SubT_{100\text{-}250m}$ and $SubT_{Kim2012}$ which we, based on above argumentation (see section 1.1, 1.2) argue to present most realistic slopes in the high temperature end of the Paleogene tropics, are plotted in Fig. S8. To provide a conservative error estimate regarding SST variability, we utilize the range between TEX_{86}^{H}, being a 0 m surface ocean endmember, and the $SubT_{100\text{-}250m}$ as appropriate range of possible SST variability. This range is used in the main text as error range for calculation of PA factors.

2. Polar amplification assessment

We used the ratio of temperature variability in the tropical surface ocean compared to open ocean bottom water temperatures (BWTs) to assess PA, consistent with previous work (Cramwinckel et al., 2018). The BWTs are derived from the benthic oxygen isotope data as provided in the CENOGRID compilation by Westerhold et al. (2020). We followed the recommendations by Hollis et al. (2019): δ^{18}O-temperature calibration using the equation of (Kim and O'Neil, 1997) as modified by Bemis et al. (1998), and an ice-free $\delta^{18}O_{sw}$ of -1.0‰ (Standard Mean Ocean Water; SMOW) and a -0.27‰ conversion factor from SMOW to VPDB (Hut, 1987). We assume a constant analytical error of 0.36 ºC (0.08‰), based on the maximum published error of the δ^{18}O data included in the CENOGRID between 54 and 52 Ma (i.e. Littler et al., 2014; Lauretano et al., 2015, 2018; Thomas et al., 2018). Absolute δ^{18}O-based BWT reconstructions are currently challenged by recent advances in carbonate clumped isotope thermometry (Meckler et al., 2022). However, clumped isotope data support the magnitude of early Eocene BWT variability from δ^{18}O-based estimates (Agterhuis et al., 2022). The long timespan, high resolution, and combination of multiple locations of the CENOGRID makes this record most appropriate for our study. However, the amplitude of short-term variability might be slightly dampened compared to single-site BWT records (Fig. S5). The dampened variability may imply that comparison to the CENOGRID gives a conservative estimate of PA.

Calculation of (orbital-scale) PA by comparing tropical TEX_{86}-derived SST variability from Site 959 to the benthic δ^{18}O-derived BWT variability from the CENOGRID compilation (Westerhold et al., 2020) relies on multiple underlying assumptions. Principally, we assume that the variability captured in the TEX_{86} signal retrieved from sedimentary sequences of Site 959 represents the SST variability of the complete tropical band. This assumption is justified by the closely related SST variability at Site 959 and the whole tropical band in the DeepMIP climate model ensemble (Fig. S1). Moreover, we find no evidence for changes in local environments that might influence GDGT distributions (Fig. S2) and also our palynological associations indicate stable open marine conditions throughout the studied interval (Fig. S4). Other assumptions include that we assume no (post)depositional processes that reduce the variability of the record on the studied time scale (>~9 cm; 20 kyr). For the deep ocean temperature signal, we assume that the amplitude of variability equals that of the high-latitude Southern Ocean throughout the studied interval. Relatively stable deep-water formation throughout the early Eocene is suggested by general consistency between benthic foraminifer δ^{18}O and δ^{13}C records of the Atlantic and Pacific ocean basins (Westerhold et al., 2018). Furthermore, deep-water formation within the DeepMIP model ensemble is relatively insensitive for pCO_2 changes in the range of early Eocene hyperthermals (Zhang et al., 2022).

Polar amplification was calculated by three different methods, with increasing reliance on stratigraphic correlation. As a first order approach of comparing short-term variability, the standard deviations (SDs) of the (1-myr LOESS) detrended records were compared. For the second approach we compared the magnitudes of correlated warming events by a Deming-regression analysis, which included propagated analytical errors of both paleotemperature records to calculate PA for both the SST and SubT datasets. The reported errors of the PA factors represent the standard errors of the associated Deming regression slopes.

For comparison with the PETM data published estimates of tropical surface warming (Frieling et al., 2017, 2019) and bottom water warming (Dunkley Jones et al., 2013) were used.

Third, we calculated PA by directly comparing the SST and BWT records in time bins. First, the optimal binning interval was determined based on the criteria that it records climate variability in the 100-kyr-eccentricity band and includes the maximum number of bins with three or more datapoints. The optimum bin size, based on the highest number of bins and included datapoints, lies close to 20 kyr (Fig. S9), which is above Nyquist frequency for short-term (100-kyr) eccentricity. Therefore, a bin size of 20-kyr was applied for the dataset, resulting in 31 bins for Site 959, after excluding all bins that include less than 3 data points. Next, a Deming regression analysis was performed between both binned datasets, incorporating the SD resulted from binning. Note that different bin sizes around the optimum do not result in large offsets in calculated PA (Fig. S9c–d). The same approach was followed for the binning of the long-term datasets in Main Text Fig 4a, but with a bin size of 1 Myr. For all three methods of PA calculation, the range between SST- and SubT-based PA was used as estimate of final error range, to cover calibration uncertainty (Section 1).

Modelled-PA was calculated based on a selection of model runs from the DeepMIP ensemble, from which the output data was retrieved from (Lunt et al., 2021): COSMOS-landveg_r2413 (COSMOS), GFDL_CM2.1 (GFDL), HadCM3B_M2.1aN (HadCM3), CESM1.2_CAM5 (CESM) (Zhu et al., 2019, p. 201) and IPSLCM5A2 (IPSL) (Zhang et al., 2020). From the output data, spatially weighted, annually averaged SSTs between 30 ºN and 30 ºS was used as tropical SST, and averaged winter SST data for <60 ºS as Southern Ocean winter SST. Precision was determined by the SD of SST data within the selected latitude bands.

Supplementary Figures

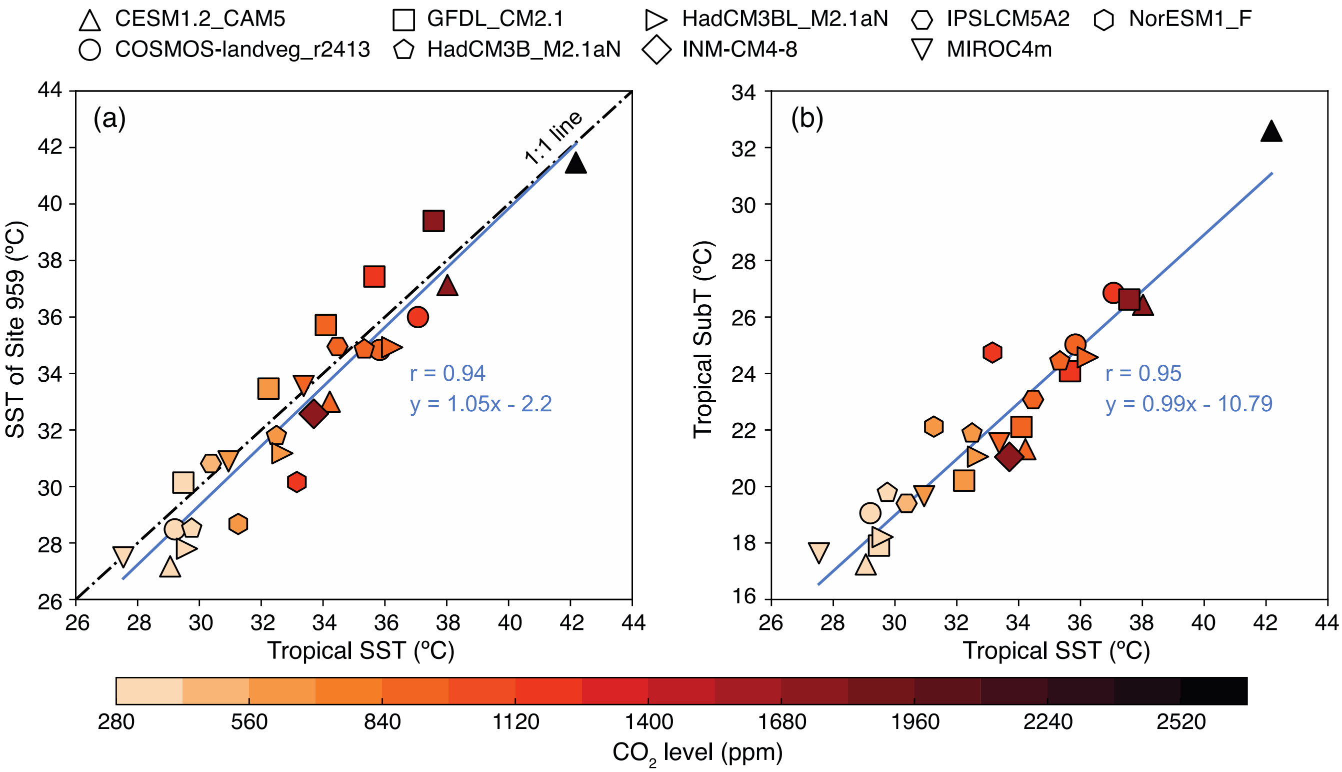

Figure S1. (Sub)surface temperature comparisons for Site 959 and the tropical band using the DeepMIP ensemble (Lunt et al., 2021). (**a**) Relation between Site 959 SST and tropical band SST. (**b**) Tropical SST versus tropical SubT (average of 100–250 m water depth). Shape and color reflect different models and CO_2 levels, respectively.

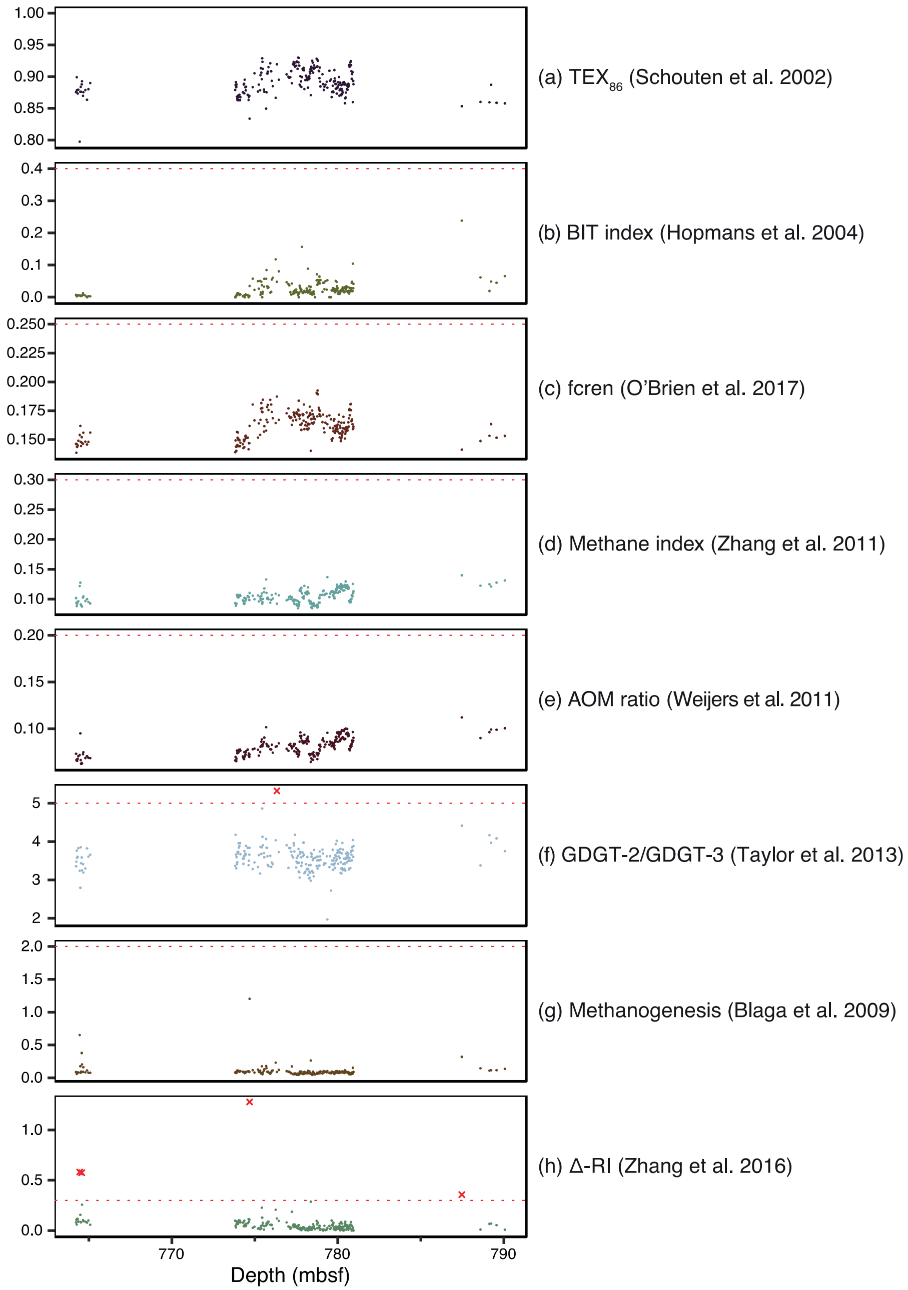

175 **Figure S2.** GDGT indices applied to detect possible overprinted TEX_{86} data. Dashed red dashed line indicates cut-off value above which data is discarded as outlier.

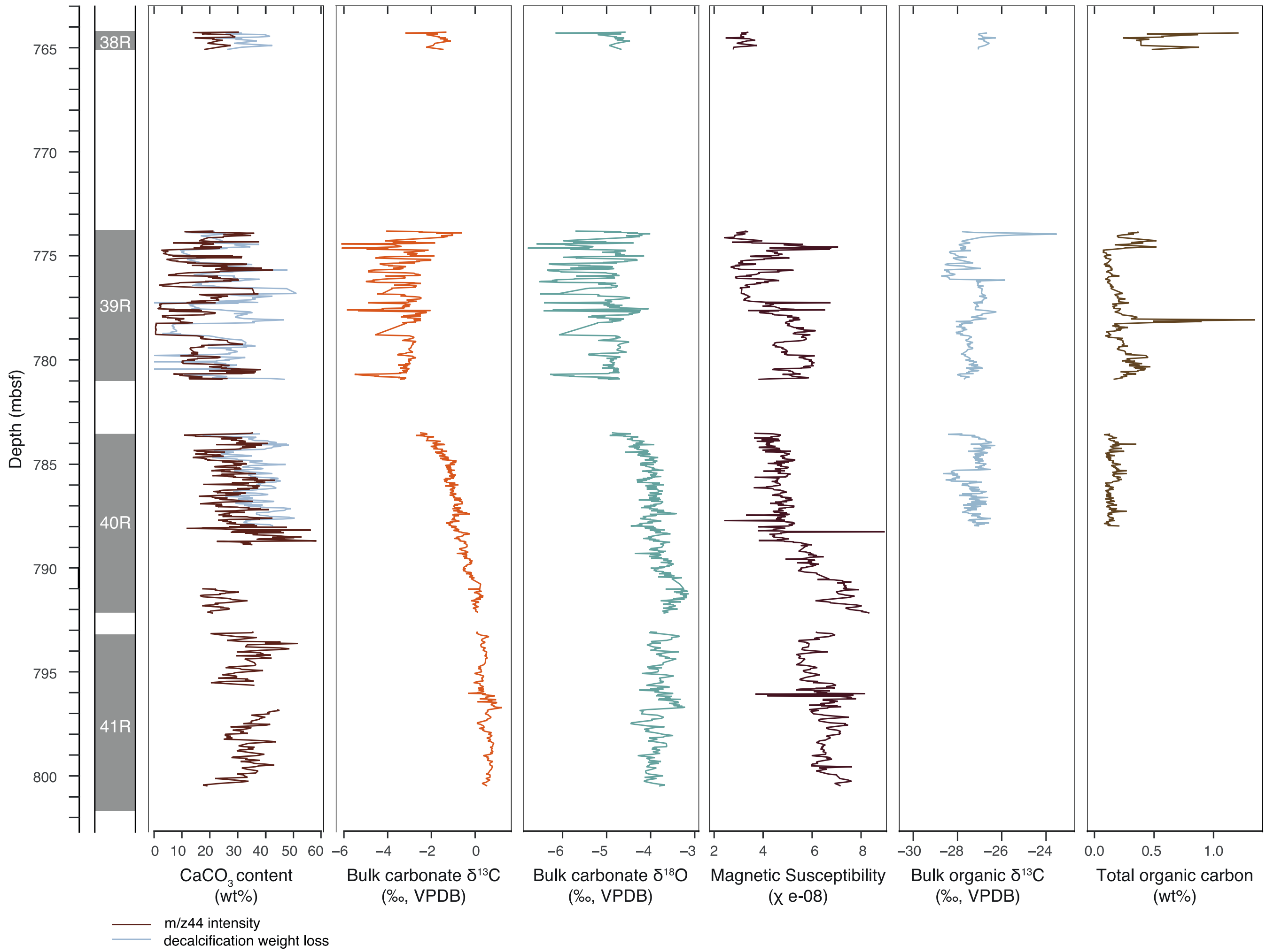

Figure S3. Bulk sediment analysis results from Site 959D Cores 41R – 38R. From left to right: $CaCO_3$ weight percent (wt%), bulk carbonate $\delta^{13}C$, bulk carbonate $\delta^{18}O$, magnetic susceptibility, bulk organic carbon $\delta^{13}C$, TOC wt% and isoprenoid GDGT concentrations.

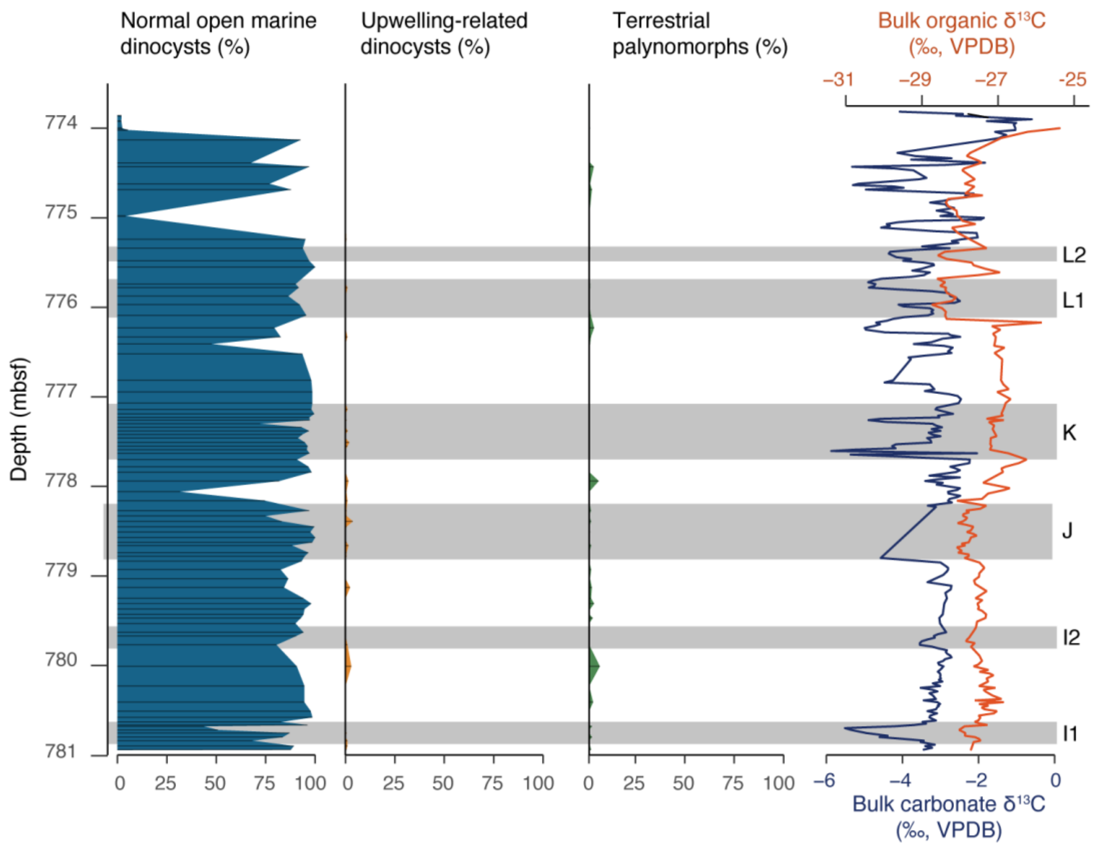

Figure S4. Palynological assemblages of Site 959 Core 39R. Groups of normal marine (including *Spiniferites* complex, fibrous Cribroperidinioids, *Operculodinium*, *Florentinia*), upwelling (i.e., protoperidinioids) and terrestrial palynomorphs (i.e., pollen and spores). On the right bulk organic (orange) and carbonate (dark blue) carbon isotope results, with globally recognized CIE events marked by grey bars.

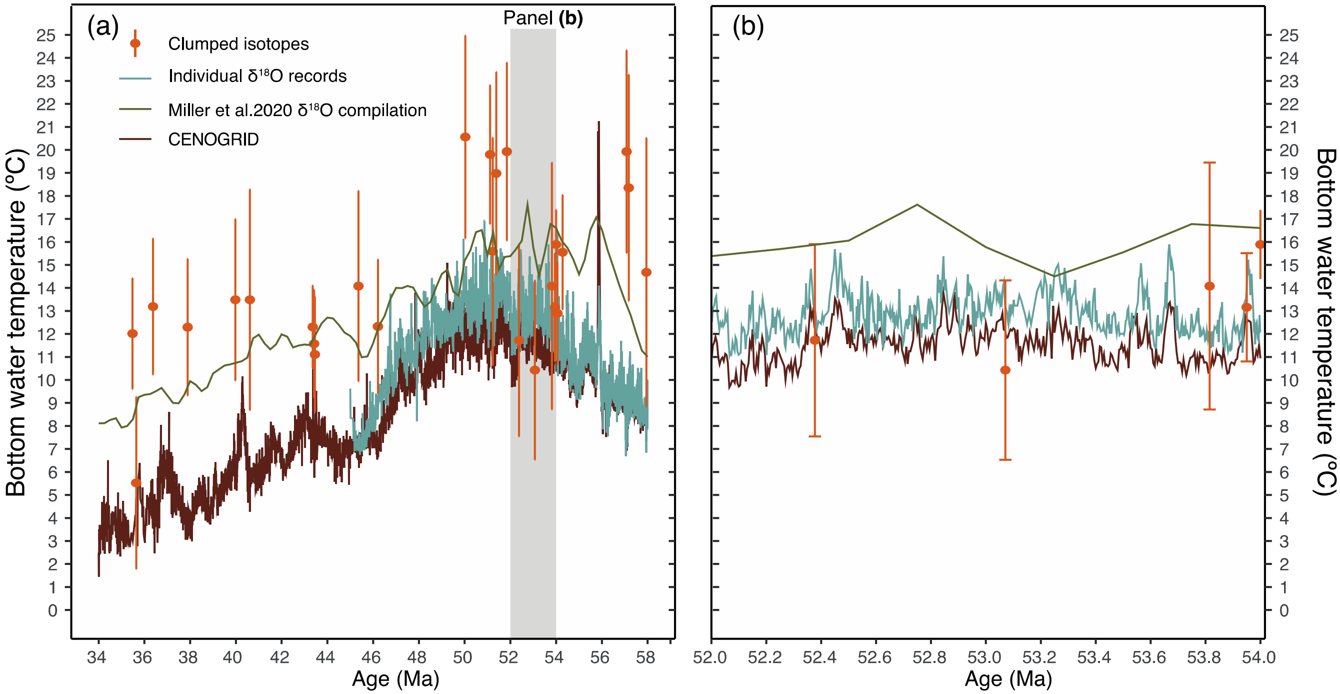

Figure S5. Various bottom water temperature reconstructions spanning the entire Eocene (**a**) and studied interval between 52 and 54 Ma (**b**). The light-blue record is calculated (see Section 3) from benthic $\delta^{18}O$ data as reported by Stap et al. (2010), Littler et al. (2014), Lauretano et al. (2015, 2018), Westerhold et al. (2018) and Thomas et al. (2018). Orange datapoints with vertical lines represent clumped isotope-based
195 temperatures with mean (points) and 95% confidence intervals (bars) (Meckler et al., 2022). Brown line indicates CENOGRID benthic compilation **(Westerhold et al., 2020)** and the green line shows the data from the **(Miller et al., 2020)** compilation.

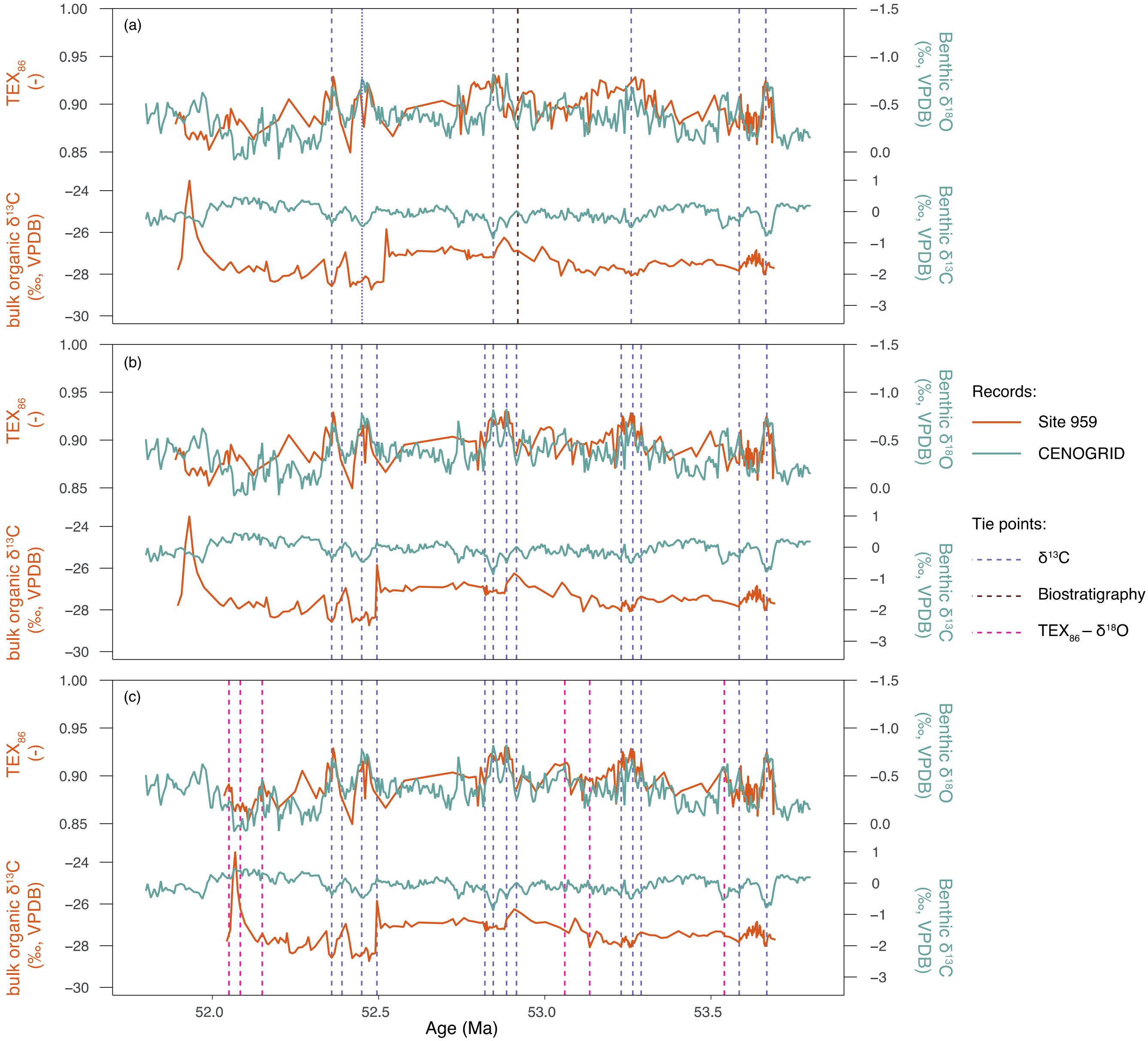

Figure S6. Finetuned correlation of Site 959 Core 39R TEX$_{86}$ and δ^{13}C record to CENOGRID benthic δ^{18}O and δ^{13}C records (Westerhold et al., 2020) for direct comparison of climate variability. (**a**) Initial correlation between Site 959 (orange) and CENOGRID (green) records based on biostratigraphy and CIEs. (**b**) Same as (**a**), but finetuned using detailed δ13Corg ties. (**c**) same as (**b**), but with additional correlations between Site 959 TEX$_{86}$ and CENOGRID benthic δ^{18}O, to optimize for direct comparison between the two climate records. Vertical dashed lines represent used tie points.

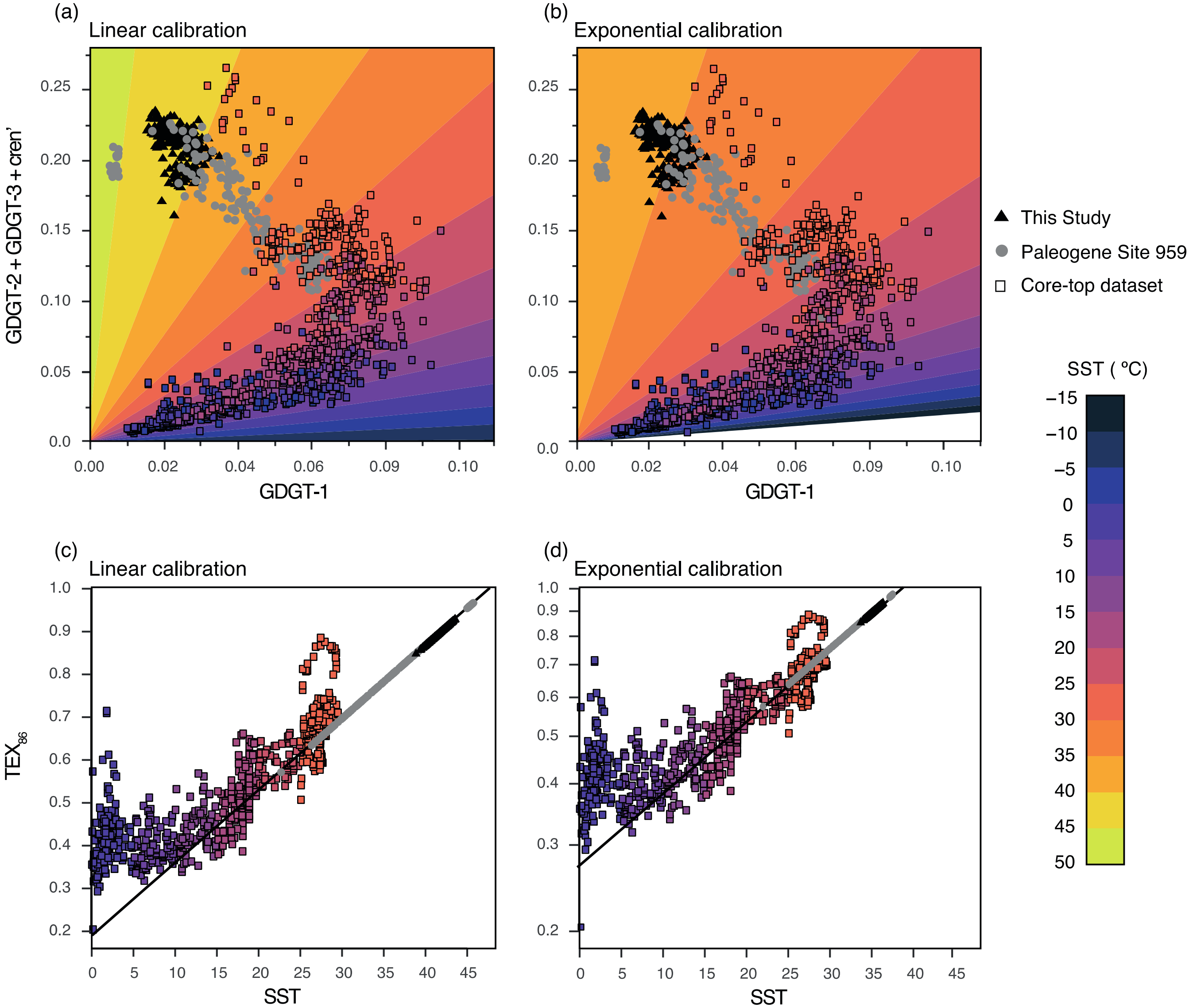

Figure S7. Fractional GDGT abundances (**a**–**b**) and SST-TEX86 relationships (**c**-**d**) for the global coretop dataset and Paleogene of Site 959. (**a**–**b**) Fractional abundance of GDGT-1 versus GDGT-2+GDGT-3+cren' (i.e. the constituents of TEX_{86}) for samples of the global coretop dataset for which these are available (Tierney and Tingley, 2015) and Site 959 Paleogene data (Cramwinckel et al., 2018; Frieling et al., 2019; This Study). Color infill of the squares represents World Ocean Atlas 2009 (Locarnini et al., 2010) SSTs as presented by Kim et al. (2010). Background colors represent calibrated SSTs based on the linear calibration by O'Brien et al. (2017) (**a**) or TEX_{86}^{H} exponential calibration by Kim et al. (2010) (**b**). (**c**–**d**) Coretop TEX_{86} values and associated SSTs as presented by Tierney and Tingley (2015). The range Paleogene Site 959 TEX_{86} data is illustrated by plotting on top of the linear (**c**) or exponential (**d**) calibration model, both represented by black lines.

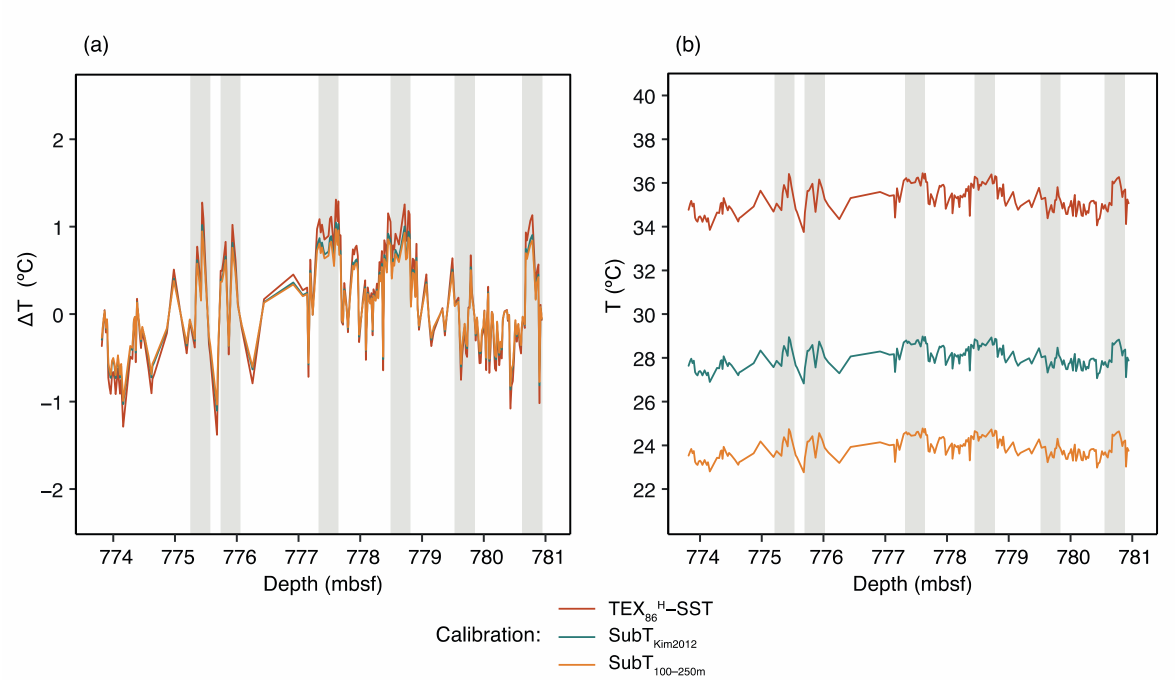

Figure S8. Results of this research using SubT and SST TEX_{86}-temperature calibrations applied to the early Eocene from Site 959. (**a**) Relative temperature changes (ΔT) for multiple calibrations after removing the mean absolute temperature. (**b**) Absolute temperatures for each calibration. Colors correspond to different calibrations.

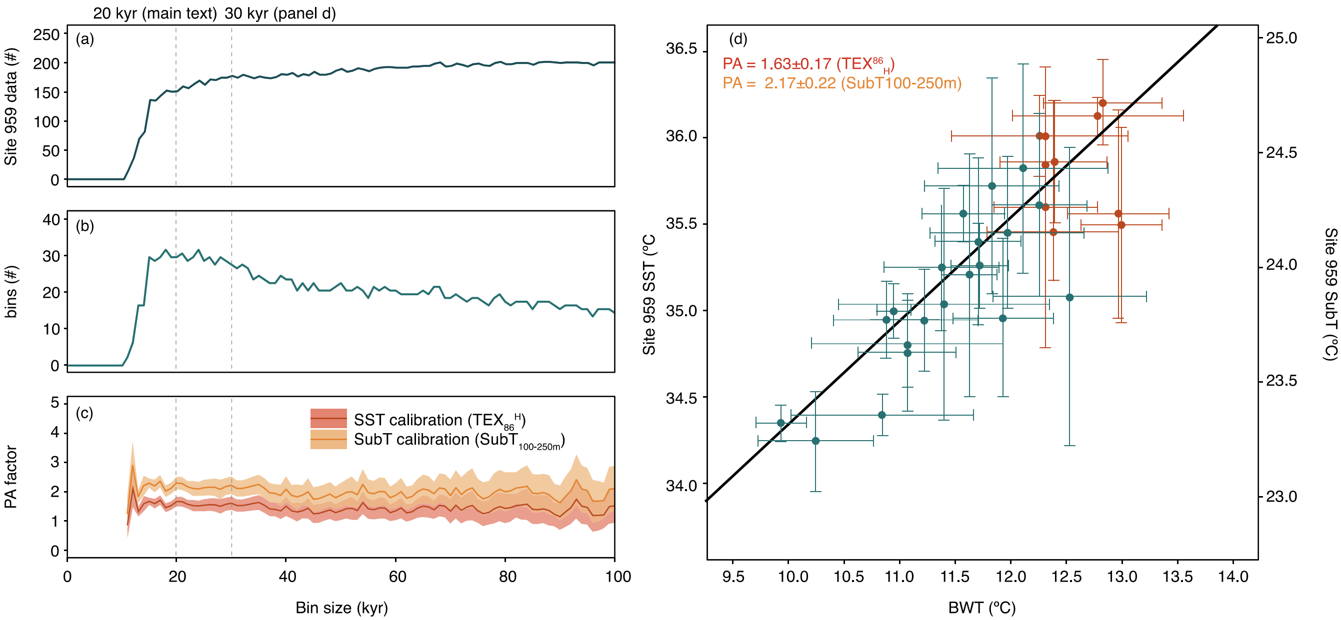

Figure S9. Bin size sensitivity analysis for PA calculation. (**a**) Number of Site 959 TEX_{86} data incorporated in the analysis, (**b**) number of bins, based on a minimum of 3 datapoints per bin and (**c**) PA factor and associated error, after calibrating Site 959 TEX_{86} data to SST (red) or SubT (orange). (**b**) Visualization of PA calculation using a bin size of 30-kyr, following the same procedure as for Fig. 2c in the main text. The black dashed line in panels (**a**–**c)** indicates the bin size of 20-kyr that is applied in the calculation of PA as presented in the main text, the grey dashed line indicates the bin size of 30-kyr, utilized to calculate PA in panel (**d**).

Supplementary References

Agterhuis, T., Ziegler, M., de Winter, N. J., and Lourens, L. J.: Warm deep-sea temperatures across Eocene Thermal Maximum 2 from clumped isotope thermometry, Commun Earth Environ, 3, 39, https://doi.org/10.1038/s43247-022-00350-8, 2022.

Bemis, B. E., Spero, H. J., Bijma, J., and Lea, D. W.: Reevaluation of the oxygen isotopic composition of planktonic foraminifera: Experimental results and revised paleotemperature equations, Paleoceanography, 13, 150–160, https://doi.org/10.1029/98PA00070, 1998.

Cramwinckel, M. J., Huber, M., Kocken, I. J., Agnini, C., Bijl, P. K., Bohaty, S. M., Frieling, J., Goldner, A., Hilgen, F. J., Kip, E. L., Peterse, F., van der Ploeg, R., Röhl, U., Schouten, S., and Sluijs, A.: Synchronous tropical and polar temperature evolution in the Eocene, Nature, 559, 382–386, https://doi.org/10.1038/s41586-018-0272-2, 2018.

Dunkley Jones, T., Lunt, D. J., Schmidt, D. N., Ridgwell, A., Sluijs, A., Valdes, P. J., and Maslin, M.: Climate model and proxy data constraints on ocean warming across the Paleocene–Eocene Thermal Maximum, Earth-Science Reviews, 125, 123–145, https://doi.org/10.1016/j.earscirev.2013.07.004, 2013.

Frieling, J., Gebhardt, H., Huber, M., Adekeye, O. A., Akande, S. O., Reichart, G.-J., Middelburg, J. J., Schouten, S., and Sluijs, A.: Extreme warmth and heat-stressed plankton in the tropics during the Paleocene-Eocene Thermal Maximum, Sci. Adv., 3, e1600891, https://doi.org/10.1126/sciadv.1600891, 2017.

Frieling, J., Peterse, F., Lunt, D. J., Bohaty, S. M., Sinninghe Damsté, J. S., Reichart, G.-J., and Sluijs, A.: Widespread Warming Before and Elevated Barium Burial During the Paleocene-Eocene Thermal Maximum: Evidence for Methane Hydrate Release?, Paleoceanography and Paleoclimatology, 34, 546–566, https://doi.org/10.1029/2018PA003425, 2019.

Hernández-Sánchez, M. T., Woodward, E. M. S., Taylor, K. W. R., Henderson, G. M., and Pancost, R. D.: Variations in GDGT distributions through the water column in the South East Atlantic Ocean, Geochimica et Cosmochimica Acta, 132, 337–348, https://doi.org/10.1016/j.gca.2014.02.009, 2014.

Ho, S. L. and Laepple, T.: Flat meridional temperature gradient in the early Eocene in the subsurface rather than surface ocean, Nature Geosci, 9, 606–610, https://doi.org/10.1038/ngeo2763, 2016.

Hollis, C. J., Dunkley Jones, T., Anagnostou, E., Bijl, P. K., Cramwinckel, M. J., Cui, Y., Dickens, G. R., Edgar, K. M., Eley, Y., Evans, D., Foster, G. L., Frieling, J., Inglis, G. N., Kennedy, E. M., Kozdon, R., Lauretano, V., Lear, C. H., Littler, K., Lourens, L., Meckler, A. N., Naafs, B. D. A., Pälike, H., Pancost, R. D., Pearson, P. N., Röhl, U., Royer, D. L., Salzmann, U., Schubert, B. A., Seebeck, H., Sluijs, A., Speijer, R. P., Stassen, P., Tierney, J., Tripati, A., Wade, B., Westerhold, T., Witkowski, C., Zachos, J. C., Zhang, Y. G., Huber, M., and Lunt, D. J.: The DeepMIP contribution to PMIP4: methodologies for selection, compilation and analysis of latest Paleocene and early Eocene climate proxy data, incorporating version 0.1 of the DeepMIP database, Geosci. Model Dev., 12, 3149–3206, https://doi.org/10.5194/gmd-12-3149-2019, 2019.

Hurley, S. J., Lipp, J. S., Close, H. G., Hinrichs, K.-U., and Pearson, A.: Distribution and export of isoprenoid tetraether lipids in suspended particulate matter from the water column of the Western Atlantic Ocean, Organic Geochemistry, 116, 90–102, https://doi.org/10.1016/j.orggeochem.2017.11.010, 2018.

Hut, G.: Consultants' group meeting on stable isotope reference samples for geochemical and hydrological investigations, International Atomic Energy Agency, Vienna., 1987.

Karner, M. B., DeLong, E. F., and Karl, D. M.: Archaeal dominance in the mesopelagiczone of thePaci®c Ocean, 409, 4, 2001.

Kim, J.-H., van der Meer, J., Schouten, S., Helmke, P., Willmott, V., Sangiorgi, F., Koç, N., Hopmans, E. C., and Damsté, J. S. S.: New indices and calibrations derived from the distribution of crenarchaeal isoprenoid tetraether lipids: Implications for past sea surface temperature reconstructions, Geochimica et Cosmochimica Acta, 74, 4639–4654, https://doi.org/10.1016/j.gca.2010.05.027, 2010.

Kim, J.-H., Romero, O. E., Lohmann, G., Donner, B., Laepple, T., Haam, E., and Sinninghe Damsté, J. S.: Pronounced subsurface cooling of North Atlantic waters off Northwest Africa during Dansgaard–Oeschger interstadials, Earth and Planetary Science Letters, 339–340, 95–102, https://doi.org/10.1016/j.epsl.2012.05.018, 2012.

Kim, S.-T. and O'Neil, J. R.: Equilibrium and nonequilibrium oxygen isotope effects in synthetic carbonates, Geochimica et Cosmochimica Acta, 61, 3461–3475, https://doi.org/10.1016/S0016-7037(97)00169-5, 1997.

Lauretano, V., Littler, K., Polling, M., Zachos, J. C., and Lourens, L. J.: Frequency, magnitude and character of hyperthermal events at the onset of the Early Eocene Climatic Optimum, Clim. Past, 11, 1313–1324, https://doi.org/10.5194/cp-11-1313-2015, 2015.

Lauretano, V., Zachos, J. C., and Lourens, L. J.: Orbitally Paced Carbon and Deep-Sea Temperature Changes at the Peak of the Early Eocene Climatic Optimum, Paleoceanography and Paleoclimatology, 33, 1050–1065, https://doi.org/10.1029/2018PA003422, 2018.

Littler, K., Röhl, U., Westerhold, T., and Zachos, J. C.: A high-resolution benthic stable-isotope record for the South Atlantic: Implications for orbital-scale changes in Late Paleocene–Early Eocene climate and carbon cycling, Earth and Planetary Science Letters, 401, 18–30, https://doi.org/10.1016/j.epsl.2014.05.054, 2014.

Liu, Z., Pagani, M., Zinniker, D., DeConto, R., Huber, M., Brinkhuis, H., Shah, S. R., Leckie, R. M., and Pearson, A.: Global Cooling During the Eocene-Oligocene Climate Transition, Science, 323, 1187–1190, https://doi.org/10.1126/science.1166368, 2009.

Locarnini, R. A., Mishonov, A. V., Antonov, A. V., Boyer, T. P., Garcia, H. E., Baranova, O. K., Zweng, M. M., and Johnson, D. R.: World Ocean Atlas 2009, Volume 1: temperature. In NOAA Atlas NESDIS, in: NOAA Atlas NESDIS (ed. S. Levitus), US Government Printing Office, Washington, D. C., 1–184, 2010.

Lunt, D. J., Bragg, F., Chan, W.-L., Hutchinson, D. K., Ladant, J.-B., Morozova, P., Niezgodzki, I., Steinig, S., Zhang, Z., Zhu, J., Abe-Ouchi, A., Anagnostou, E., de Boer, A. M., Coxall, H. K., Donnadieu, Y., Foster, G., Inglis, G. N., Knorr, G., Langebroek, P. M., Lear, C. H., Lohmann, G., Poulsen, C. J., Sepulchre, P., Tierney, J. E., Valdes, P. J., Volodin, E. M., Jones, T. D., Hollis, C. J., Huber, M., and Otto-Bliesner, L.: DeepMIP: Model intercomparison of early Eocene climatic optimum (EECO) large-scale climate features and comparison with proxy data, Clim. Past, 17, 203–227, 2021.

Massana, R., DeLong, E. F., and Pedrós-Alió, C.: A Few Cosmopolitan Phylotypes Dominate Planktonic Archaeal Assemblages in Widely Different Oceanic Provinces, Appl Environ Microbiol, 66, 1777–1787, https://doi.org/10.1128/AEM.66.5.1777-1787.2000, 2000.

Meckler, A. N., Sexton, P. F., Piasecki, A. M., Leutert, T. J., Marquardt, J., Ziegler, M., Agterhuis, T., Lourens, L. J., Rae, J. W. B., Barnet, J., Tripati, A., and Bernasconi, S. M.: Cenozoic evolution of deep ocean temperature from clumped isotope thermometry, Science, 377, 86–90, https://doi.org/10.1126/science.abk0604, 2022.

Miller, K. G., Browning, J. V., Schmelz, W. J., Kopp, R. E., Mountain, G. S., and Wright, J. D.: Cenozoic sea-level and cryospheric evolution from deep-sea geochemical and continental margin records, Sci. Adv., 6, eaaz1346, https://doi.org/10.1126/sciadv.aaz1346, 2020.

O'Brien, C. L., Robinson, S. A., Pancost, R. D., Sinninghe Damsté, J. S., Schouten, S., Lunt, D. J., Alsenz, H., Bornemann, A., Bottini, C., Brassell, S. C., Farnsworth, A., Forster, A., Huber, B. T., Inglis, G. N., Jenkyns, H. C., Linnert, C., Littler, K., Markwick, P., McAnena, A., Mutterlose, J., Naafs, B. D. A., Püttmann, W., Sluijs, A., van Helmond, N. A. G. M., Vellekoop, J., Wagner, T., and Wrobel, N. E.: Cretaceous sea-surface temperature evolution: Constraints from TEX_{86} and planktonic foraminiferal oxygen isotopes, Earth-Science Reviews, 172, 224–247, https://doi.org/10.1016/j.earscirev.2017.07.012, 2017.

Rattanasriampaipong, R., Zhang, Y. G., Pearson, A., Hedlund, B. P., and Zhang, S.: Archaeal lipids trace ecology and evolution of marine ammonia-oxidizing archaea, Proc. Natl. Acad. Sci. U.S.A., 119, e2123193119, https://doi.org/10.1073/pnas.2123193119, 2022.

Schouten, S., Hopmans, E. C., Schefuß, E., and Sinninghe Damsté, J. S.: Distributional variations in marine crenarchaeotal membrane lipids: a new tool for reconstructing ancient sea water temperatures?, Earth and Planetary Science Letters, 204, 265–274, https://doi.org/10.1016/S0012-821X(02)00979-2, 2002.

Sinninghe Damsté, J. S., Rijpstra, W. I. C., Hopmans, E. C., Prahl, F. G., Wakeham, S. G., and Schouten, S.: Distribution of Membrane Lipids of Planktonic *Crenarchaeota* in the Arabian Sea, Appl Environ Microbiol, 68, 2997–3002, https://doi.org/10.1128/AEM.68.6.2997-3002.2002, 2002.

Stap, L., Lourens, L. J., Thomas, E., Sluijs, A., Bohaty, S., and Zachos, J. C.: High-resolution deep-sea carbon and oxygen isotope records of Eocene Thermal Maximum 2 and H2, Geology, 38, 607–610, https://doi.org/10.1130/G30777.1, 2010.

Taylor, K. W. R., Huber, M., Hollis, C. J., Hernandez-Sanchez, M. T., and Pancost, R. D.: Re-evaluating modern and Palaeogene GDGT distributions: Implications for SST reconstructions, Global and Planetary Change, 108, 158–174, https://doi.org/10.1016/j.gloplacha.2013.06.011, 2013.

Thomas, E., Boscolo-Galazzo, F., Balestra, B., Monechi, S., Donner, B., and Röhl, U.: Early Eocene Thermal Maximum 3: Biotic Response at Walvis Ridge (SE Atlantic Ocean), Paleoceanography and Paleoclimatology, 33, 862–883, https://doi.org/10.1029/2018PA003375, 2018.

Tierney, J. E. and Tingley, M. P.: A Bayesian, spatially-varying calibration model for the TEX_{86} proxy, Geochimica et Cosmochimica Acta, 127, 83–106, https://doi.org/10.1016/j.gca.2013.11.026, 2014.

Tierney, J. E. and Tingley, M. P.: A TEX_{86} surface sediment database and extended Bayesian calibration, Sci Data, 2, 150029, https://doi.org/10.1038/sdata.2015.29, 2015.

Tierney, J. E., Sinninghe Damsté, J. S., Pancost, R. D., Sluijs, A., and Zachos, J. C.: Eocene temperature gradients, Nature Geosci, 10, 538–539, https://doi.org/10.1038/ngeo2997, 2017.

Villanueva, L., Schouten, S., and Sinninghe Damsté, J. S.: Depth-related distribution of a key gene of the tetraether lipid biosynthetic pathway in marine Thaumarchaeota: Distribution of a thaumarchaeotal lipid enzyme, Environ Microbiol, 17, 3527–3539, https://doi.org/10.1111/1462-2920.12508, 2015.

van der Weijst, C. M. H., Winkelhorst, J., de Nooijer, W., von der Heydt, A., Reichart, G.-J., Sangiorgi, F., and Sluijs, A.: Pliocene evolution of the tropical Atlantic thermocline depth, Clim. Past, 18, 961–973, https://doi.org/10.5194/cp-18-961-2022, 2022.

Westerhold, T., Röhl, U., Donner, B., and Zachos, J. C.: Global Extent of Early Eocene Hyperthermal Events: A New Pacific Benthic Foraminiferal Isotope Record From Shatsky Rise (ODP Site 1209), Paleoceanography and Paleoclimatology, 33, 626–642, https://doi.org/10.1029/2017PA003306, 2018.

Westerhold, T., Marwan, N., Drury, A. J., Liebrand, D., Agnini, C., Anagnostou, E., Barnet, J. S. K., Bohaty, S. M., De Vleeschouwer, D., Florindo, F., Frederichs, T., Hodell, D. A., Holbourn, A. E., Kroon, D., Lauretano, V., Littler, K., Lourens, L. J., Lyle, M., Pälike, H., Röhl, U., Tian, J., Wilkens, R. H., Wilson, P. A., and Zachos, J. C.: An astronomically dated record of Earth's climate and its predictability over the last 66 million years, Science, 369, 1383–1387, https://doi.org/10.1126/science.aba6853, 2020.

Zakem, E. J., Al-Haj, A., Church, M. J., van Dijken, G. L., Dutkiewicz, S., Foster, S. Q., Fulweiler, R. W., Mills, M. M., and Follows, M. J.: Ecological control of nitrite in the upper ocean, Nat Commun, 9, 1206, https://doi.org/10.1038/s41467-018-03553-w, 2018.

Zhang, Y., Huck, T., Lique, C., Donnadieu, Y., Ladant, J.-B., Rabineau, M., and Aslanian, D.: Early Eocene vigorous ocean overturning and its contribution to a warm Southern Ocean, Clim. Past, 16, 1263–1283, https://doi.org/10.5194/cp-16-1263-2020, 2020.

Zhang, Y., Boer, A. M., Lunt, D. J., Hutchinson, D. K., Ross, P., Flierdt, T., Sexton, P., Coxall, H. K., Steinig, S., Ladant, J., Zhu, J., Donnadieu, Y., Zhang, Z., Chan, W., Abe-Ouchi, A., Niezgodzki, I., Lohmann, G., Knorr, G., Poulsen, C. J., and Huber, M.: Early Eocene Ocean Meridional Overturning Circulation: The Roles of Atmospheric Forcing and Strait Geometry, Paleoceanog and Paleoclimatol, 37, https://doi.org/10.1029/2021PA004329, 2022.

Zhu, J., Poulsen, C. J., and Tierney, J. E.: Simulation of Eocene extreme warmth and high climate sensitivity through cloud feedbacks, Sci. Adv., 5, eaax1874, https://doi.org/10.1126/sciadv.aax1874, 2019.